J. Fluid Mech. (2000), *vol.* 418, *pp.* 137–166. Printed in the United Kingdom

Reconstruction of the global velocity field in the axisymmetric mixing layer utilizing the proper orthogonal decomposition

By J. H. CITRINITI AND W. K. GEORGE

Department of Mechanical and Aerospace Engineering, State University of New York at Buffalo, Buffalo, NY 14260, USA

(Received 23 May 2000)

Experimental data are presented from 138 synchronized channels of hot-wire anemometry in an investigation of the large-scale, or coherent, structures in a high Reynolds number fully developed, turbulent axisymmetric shear layer. The dynamics of the structures are obtained from instantaneous realizations of the streamwise velocity field in a single plane, $x/D = 3$, downstream of a round jet nozzle. The Proper Orthogonal Decomposition (POD) technique is applied to an ensemble of these realizations to determine optimal representations of the velocity field, in a mean-square sense, in terms of an orthogonal basis. The coefficients of the orthogonal functions, which describe the temporal evolution of the POD eigenfunctions, are determined by projecting instantaneous realizations of the velocity field onto the basis.

Evidence is presented to show that with a partial reconstruction of the velocity field, using only the first radial POD mode, the large-scale structure is objectively educed from the turbulent field. Further, it is shown that only five azimuthal Fourier modes (0,3,4,5,6) are necessary to represent the evolution of the large-scale structure. The results of the velocity reconstruction using the POD provide evidence for azimuthally coherent structures that exist near the potential core. In addition to the azimuthal structures near the potential core, evidence is also found for the presence of counter-rotating, streamwise vortex pairs (or ribs) in the region between successive azimuthally coherent structures as well as coexisting for short periods with them. The large-scale structure cycle, which includes the appearance of the ring structure, the advection of fluid by the ribs in the braid region and their advection toward the outside of the layer by a following ring structure, repeats approximately every one integral time scale. One surprising result was that the most spatially correlated structure in the flow, the coherent ring near the potential core which ejects fluid in the streamwise direction in a volcano-like eruption, is also the one with the shortest time scale.

1. Introduction

Large-scale structures in turbulent flows have been known to exist for a number of years but their contribution to the dynamics of turbulent motion has only recently been investigated. The wealth of knowledge on the structure in the plane mixing layer (see Winant & Browand 1974; Browand & Weidman 1976; Breidenthal 1981; Pierrehumbert & Widnall 1982; Bernal & Roshko 1986; Lasheras, Cho & Maxworthy 1986; Corcos & Sherman 1984; Corcos & Lin 1984; Lin & Corcos 1984; Metcalfe *et al.* 1987; and Rogers & Moser 1992) has produced a theory for the life cycle of the coherent structures in the layer. The layer is dominated by spanwise vortices,

or 'rollers', of the Kelvin–Helmholtz type which control growth and mixing in the layer. Streamwise-oriented rib vortices develop in the high-strain braid region between consecutive spanwise rollers. The streamwise ribs, in some cases, collapse into compact, round vortex tubes. The ribs are not very dynamic and are considered passive entities which do not contribute much to the mixing and growth of the layer (Lin & Corcos 1984), these aspects being dominated by the spanwise roller. The formation of the rib vorticity is, however, considered one signal of the transition to turbulence (Rogers & Moser 1992).

The state of knowledge of large-scale structure dynamics in the near field of the axisymmetric jet is, unlike the plane layer, much less advanced. The literature in this area begins with the work of Crow & Champagne (1971) who suggested that the jet shear layer contains orderly vortical structure. Subsequent measurements by Yule (1978) using conditional sampling techniques led to the concept that the vortical structure interacts and coalesces. Further indication of this is given by Lau & Fisher (1975) who proposed a 'vortex street' model for the evolution of the azimuthal rings.

Flow visualization experiments concentrating on high-Reynolds-number turbulent jets by Hussain & Clark (1981) demonstrated the presence of coherent structures in situations more typical of engineering flows. Further work by Hussain and his coworkers using controlled excitation in combination with conditional sampling techniques (reviewed in Hussain 1986) confirmed the existence of azimuthal vortex pairing and produced detailed topographical measurements of the coherent rings. Vortex pairing was found to occur in two distinct modes, the jet column mode and the shear layer mode, the determination of which is based on the Strouhal number.

In the past five or six years, a great deal of effort in the study of large-scale structures in the jet shear layer has focused on the role streamwise vorticity plays in the shear layer dynamics. The streamwise structure is similar to that found in the plane mixing layer, i.e. pairs of counter-rotating rib vortices with predominately streamwise orientation are formed in the high-strain braid region between azimuthally coherent rings. The work of Liepmann (1991) and Liepmann & Gharib (1992) demonstrated the importance of the streamwise vorticity in the mixing processes in the layer, especially near the end of the potential core. Their DPIV and LIF visualizations of a relatively low-Reynolds-number mixing layer show the clear presence of streamwise ribs in the braid region and their entrainment measurements demonstrate the importance of the streamwise structure in the mixing processes of the layer. Martin & Meiburg (1991) show how two competing induction effects control the formation of the streamwise structure and how they become wound into the core of the azimuthal rings.

Streamwise vortices have also been seen in a high-Reynolds-number jet by Paschereit *et al.* (1992) but their interaction and evolution was not considered. An experimental and numerical investigation into the dynamics of the streamwise structures was performed by Grinstein *et al.* (1995*b*), who suggest that this structure is an important mechanism in the breakdown to three-dimensional turbulence and therefore for increased molecular mixing. Their numerical simulations also show the clear presence of streamwise ribs in the braid region and the authors discuss the effect of these ribs on the combustion process in the mixing layer.

What is missing in the above studies is a detailed study of the temporal sequencing of the naturally occurring large-scale structure in the axisymmetric mixing layer. The difficulty in utilizing the techniques mentioned above is that it is not possible to truly study the structure dynamics because of the inability of the various techniques to objectively define the large-scale structure. Only after the structure is rigorously defined can its evolution be accurately described. For instance, the conditional sampling

technique requires that the structure be phase locked in space so that sufficient statistical measures of the structure can be made. Flow visualization techniques do not normally have the sampling rate necessary to handle high-Reynolds-number structure interaction, though they can be used to study these processes at low Reynolds numbers (Liepmann & Gharib 1992). However, to understand the structure dynamics at a Reynolds number typical of engineering applications another technique needs to be introduced.

In 1967 Lumley proposed a method by which the most energetic structures of a turbulent flow field could be objectively recovered. Called the Proper Orthogonal Decomposition or POD, Lumley suggested that the large-scale, or coherent, structure occurs in an identifiable manner in a given ensemble of random vector fields, and this structure makes a significant contribution to the total kinetic energy in the field. Lumley further suggested that the lowest-order eigenfunction be identified with the large-scale structure. Glauser & George (1987) (see also George 1988) subsequently modified Lumley's hypothesis and suggested instead that the POD merely represented an optimal basis for examining the life cycle of the coherent structures, with different eigenfunctions representing it at various times in its life cycle. In this view, not only were the POD eigenfunctions of interest, but also the coefficients which turned the POD modes on and off at various points in the structure evolution.

In the late 1970s an ambitious project began at SUNY at Buffalo to utilize the POD to extract the large-scale structure in the jet mixing layer without having to use controlled excitation of the layer. The results of this work are presented in Glauser (1987), Glauser, Leib & George (1987) and Grinstein, Glauser & George (1995*a*) (collectively referred to as I in the remainder of this article). The integral eigenvalue equation resulting from the application of the POD to the axisymmetric jet mixing layer was solved experimentally in (I). The most energetic structure recovered by the POD in this decomposition contained 40% of the total turbulent kinetic energy in the flow with the second and third structures combining to contribute another 40%.

It was suggested that the *naturally occurring* coherent structures in the field behave much like the interaction of two round vortices in which the trailing vortex is pulled through the centre of the leading ring in a classic leap-frog effect. As the second ring is pulled through the first, it enlarges the radius of the first causing its core diameter to shrink and making it more susceptible to instabilities in the azimuthal direction. This outer ring develops a wavy azimuthal shape which is stretched and bent by the mean velocity field, aligning the vorticity vector with the mean flow in some positions. The result is a strong 'ring' structure near the potential core with less azimuthally coherent vorticity in the outer part of the layer.

One interesting observation of the Glauser *et al.* (1987) experiment was the similarity between the full vector POD decomposition and the streamwise-only decomposition, i.e. most of the information obtained in the full vector decomposition was available in the streamwise-only decomposition. This prompted the present experiment which focused only on the streamwise velocity field in the application of the POD, thereby reducing the complexity of the experimental investigation to a level which made an attempt at recovering the instantaneous dynamics of the POD modes feasible.

This paper reports on the results of an application of the POD to the streamwise velocity field in the axisymmetric mixing layer utilizing 138 simultaneously operating hot-wire anemometer probes. Life cycles of the dynamic events extracted using the POD are presented in §§ 5.3–5.4, following a brief description of the POD, the experiment and the data analysis techniques.

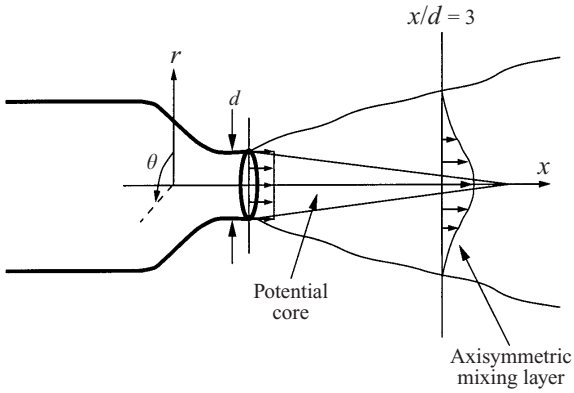

FIGURE 1. Schematic of the jet mixing layer.

2. Proper orthogonal decomposition

2.1. *General decomposition*

The Proper Orthogonal Decomposition seeks the most energetic fluctuations in a random vector field, and in turbulent flow the vector field of interest is the instantaneous velocity $u_i(\boldsymbol{x}, t)$. The POD basis functions, $\varphi_i(\boldsymbol{x}, t)$ are defined by the maximization of their normalized mean-square projection on the velocity vector (Lumley 1967; Holmes, Lumley & Berkooz 1996):

$$\frac{\left\langle \int u_i(\boldsymbol{x}, t)\varphi_i^*(\boldsymbol{x}, t)\mathrm{d}\boldsymbol{x}\,\mathrm{d}t \int \left[u_j(\boldsymbol{x}', t)\varphi_j^*(\boldsymbol{x}', t)\right]^* \mathrm{d}\boldsymbol{x}'\mathrm{d}t \right\rangle}{\int \varphi_l(\boldsymbol{x}, t)\varphi_l^*(\boldsymbol{x}, t)\mathrm{d}\boldsymbol{x}\,\mathrm{d}t} = \lambda, \tag{2.1}$$

where the asterisk denotes complex conjugation and angle brackets denote ensemble averaging. The normalization of the projection is done to eliminate amplitude dependence on the resulting functions and instead emphasize the degree of the projection.

The maximization of λ is performed via the calculus of variations and the result is an integral eigenvalue equation of the Fredholm type (Lumley 1967),

$$\int R_{i,j}(\boldsymbol{x}, \boldsymbol{x}', t, t')\varphi_j(\boldsymbol{x}', t')\mathrm{d}\boldsymbol{x}'\mathrm{d}t' = \lambda\varphi_i(\boldsymbol{x}, t), \tag{2.2}$$

where the symmetric kernel of this equation is the two-point correlation tensor

$$R_{i,j}(\boldsymbol{x}, \boldsymbol{x}', t, t') = \langle u_i(\boldsymbol{x}, t)u_j(\boldsymbol{x}', t')\rangle. \tag{2.3}$$

The solution to equation (2.2) for fields of finite total energy, i.e. statistically inhomogeneous fields, and symmetric kernels is governed by the Hilbert Schmidt theory of linear integral equations.

2.2. *Axisymmetric mixing layer*

The axisymmetric mixing layer formed at the exit of a round jet as the high-velocity fluid exiting a round nozzle creates a turbulent shear layer with the quiescent fluid into which it flows. A schematic of the axisymmetric mixing layer is shown in figure 1 and the coordinate definitions for this analysis are $(x_1, x_2, x_3) = (x, r, \theta)$. For this application, the streamwise coordinate was fixed at a position 3 diameters downstream

of the jet exit. Therefore the implicit dependence on the streamwise, or x-direction has been dropped.

The velocity field in the mixing layer is statistically stationary in time and therefore the POD eigenfunctions are the familiar harmonic functions. The statistical properties of the velocity vector in the azimuthal direction of the mixing layer are axisymmetric (I and Sreenivasan 1984). Consequently, periodic functions in this direction are then discrete Fourier modes. It is then easier to Fourier transform the time signal (using an FFT) and work with the double Fourier transform given by

$$\hat{u}_i(r,m,f) = \int_0^\infty \int_0^\infty \mathrm{e}^{-\mathrm{i}(2\pi f t + m\theta)} u(r,\theta,t)\,\mathrm{d}\theta\,\mathrm{d}t. \tag{2.4}$$

From this, the two-point cross-spectrum $S_{i,j}(r,r',m,f)$ can be formed with

$$S_{i,j}(r,r',m,f) = \langle \hat{u}_i(r,m,f)\hat{u}_j^*(r',m,f)\rangle. \tag{2.5}$$

The integral eigenvalue equation for the POD for this flow is then given by

$$\int S_{i,j}(r,r',m,f)\varphi_j(r',m,f)r'\mathrm{d}r' = \lambda(m,f)\varphi_i(r,m,f). \tag{2.6}$$

In order to make the kernel Hermitian symmetric with respect to the integrand, which is a requirement of the Hilbert–Schmidt theory (Lumley 1970) we define

$$B_{i,j}(r,r',m,f) = r^{1/2}S_{i,j}(r,r',m,f)r'^{1/2} \tag{2.7}$$

and

$$\phi_i(r,m,f) = r^{1/2}\varphi_i(r,m,f) \tag{2.8}$$

so that the integral equation (2.6) becomes

$$\int B_{i,j}(r,r',m,f)\phi_j(r',m,f)\mathrm{d}r' = \lambda(m,f)\phi_i(r,m,f), \tag{2.9}$$

where λ is now an eigenspectrum, decomposed into azimuthal Fourier modes.

Equation (2.9) is now a homogeneous integral equation of the second kind. For fixed limits of integration it is referred to as a Fredholm equation and the Hilbert–Schmidt theory provides a series of useful properties for the eigenvalues and eigenfunctions:

(*a*) There exists a denumerable set of discrete solutions to equation (2.9) ($\phi_i^{(n)}$ corresponding to the eigenvalues $\lambda^{(n)}$) so equation (2.9) may be written

$$\int B_{i,j}(r,r',m,f)\phi_j^{(n)}(r',m,f)\mathrm{d}r' = \lambda^{(n)}(m,f)\phi_i^{(n)}(r,m,f), \tag{2.10}$$

where $n = 1,2,3\ldots$ represents the discrete nature of the solution set.

(*b*) The eigenvalues are real and ordered such that

$$\lambda^{(1)}(m,f) > \lambda^{(2)}(m,f) > \lambda^{(3)}(m,f)\ldots. \tag{2.11}$$

(*c*) The eigenfunctions are orthogonal and can be normalized so that

$$\int \phi_i^{(p)}(r,m,f)\phi_i^{(q)}(r,m,f)\mathrm{d}r = \delta_{pq}. \tag{2.12}$$

(*d*) The velocity field, decomposed into azimuthal modes m and frequency f, can be expressed as a linear combination of the eigenfunctions, i.e.

$$r^{1/2}\hat{u}_i^{nmf}(r,m,f) = \sum_{n=1}^{N} \hat{a}_n(m,f)\phi_i^{(n)}(r,m,f), \tag{2.13}$$

where the 'hat' superscript is used to indicate a transformed quantity and the m, f superscripts indicate which transformations have been performed, i.e. azimuthal mode and frequency respectively. The n superscript is to emphasize that the velocity is reconstructed from the eigenfunctions. The random coefficients are obtained using the orthogonality of the eigenfunctions, i.e.

$$\hat{a}_n(m,f) = \int r^{1/2}\hat{u}_i^{nmf}(r,m,f)\phi_i^{(n)*}(r,m,f)\mathrm{d}r. \tag{2.14}$$

(*e*) The turbulent kinetic energy is the sum of the eigenvalues (see equations (2.12) and (2.13))

$$E = \int \langle \hat{u}_i^{nmf}(r,m,f)\hat{u}_i^{nmf*}(r,m,f)\rangle \mathrm{d}r = \sum_n \sum_m \int_f \lambda^{(n)}(m,f)\mathrm{d}f. \tag{2.15}$$

An important property of the eigenfunctions obtained via the POD is illustrated by equation (2.15). Since the eigenvalues are known to be ordered (see (*b*) above) and the sum over all eigenvalues gives the total turbulent kinetic energy in the flow, the first eigenvalue will contain the largest amount of kinetic energy and successive eigenvalues will contain a decreasing amount, i.e. the energy in the flow has been recovered in an optimal manner. This implies that the first (or first few) POD mode(s) can be used to represent the 'large eddies' in the flow. For more on this aspect of the POD, a summary of the relationship between the POD eigenfunctions and flow structure is given by George (1988) and Moin & Moser (1989).

2.2.1. *This application*

The streamwise velocity component in the axisymmetric mixing layer at $x/d = 3$ was measured at numerous radial and azimuthal locations to both recover the eigenfunctions and eigenvalues defined in equation (2.10) and perform the projection specified by equation (2.14). Since only the streamwise velocity was measured, the equations simplify to

$$\int B_{1,1}(r,r',m,f)\phi_1^{(n)}(r',m,f)\mathrm{d}r' = \lambda^{(n)}(m,f)\phi_1^{(n)}(r,m,f) \tag{2.16}$$

and

$$\hat{a}_n(m,f) = \int r^{1/2}\hat{u}_1^{nmf}(r,m,f)\phi_1^{n*}(r,m,f)\mathrm{d}r. \tag{2.17}$$

An important observation here is that unlike the cross-spectra in equation (2.16), the kernel of equation (2.17) is non-deterministic since it is the instantaneous realization of the random velocity decomposed into frequency and azimuthal mode numbers. Therefore, whereas equation (2.16) allows sequential measurements of the velocity field in order to obtain a sufficient statistical measure of the cross-spectra, in equation (2.17) the streamwise velocity must be measured *simultaneously* on a grid of sufficient spatial resolution, to retain the proper phase relationships in $\hat{u}_1^{nmf}(r,m,f)$. This requirement for simultaneous measurement and the experimental difficulties it presented were the primary reasons for performing the experiment at only a single downstream location and measuring only one component of the velocity vector. The probe array designed to accomplish this task is described in detail in § 3.2.3.

2.3. *Numerical approximation*

Since the kernel in equation (2.16) can be known only at discrete positions where there are probes, the integral in the equation must be replaced by an appropriate

quadrature rule. For each m, f combination,

$$\sum_{i=1}^{N_r} B_{1,1}(r_i, r_j)\phi_1^{(n)}(r_i)H_i = \lambda^n \phi_1^{(n)}(r_j), \tag{2.18}$$

where N_r is the number of radial measuring positions and H_i is the quadrature weighting function defined by

$$H_i = \frac{\Delta r}{3} k_i \tag{2.19}$$

where

$$\Delta r = \frac{r_o - r_i}{N_r - 1} \tag{2.20}$$

is the grid spacing in r and k_i is the weighting factor.

Similarly, the equation for the coefficients of the POD eigenfunctions is,

$$\hat{a}_n(m, f) = \sum_{i=1}^{N_r} r^{1/2} \hat{u}_1^{nmf}(r_i, m, f)\phi_1^{(n)*}(r_i, m, f)H_i. \tag{2.21}$$

2.4. *Numerical implementation*

This application of the POD required the double-transformed, instantaneous velocity, $\hat{u}_1^{nmf}(r, m, f)$, for the determination of the random coefficients, $\hat{a}_n(m, f)$ (see equation (2.21)) and for calculation of the kernel in equation (2.18). It was computationally advantageous to first transform the original velocity signals from all probes in time and decompose them into azimuthal Fourier modes.

The procedure for calculating the double-transformed velocity and forming the POD kernel was follows. For each of the blocks of data:

(*a*) Fourier transform in time, using an FFT algorithm, the instantaneous velocity obtained from each of the 138 hot-wire probes. The result is a set of Fourier coefficients, $\hat{u}_1^k(r, \theta)$, representing the temporal transform of the streamwise velocity. The coefficients are discretely known at each of the $k = 1, 2, 3, \ldots$ frequencies where $f = k\Delta f$, $\Delta f = 1/T$ and T is the record length of each block.

(*b*) For each radius in the measurement grid (see figure 2 below), carry out a spatial decomposition of the Fourier coefficients in (*a*) to create a double-decomposed velocity, $\hat{u}_1^{lk}(r)$. Note that this is a complex Fourier transform since the Fourier coefficients in (*a*) were complex. The result is another set of Fourier coefficients, $\hat{u}_1^{lk}(r)$, representing the double-transformed velocity. The discrete mode number, $l = 1, 2, 3, \ldots$, is given by $m = l\Delta\theta$ where $\Delta\theta = 2\pi/N_\theta$ and N_θ is the number of azimuthal probe positions at each radius (figure 2).

(*c*) With the results of (*b*), form the kernel of equation (2.18) using its estimator given by

$$B_{1,1}^E(r_i, r_j) = \frac{\langle \hat{u}_1^{lk}(r_i)\hat{u}_1^{lk*}(r_j)\rangle}{T}, \tag{2.22}$$

where the E superscript signifies an estimator of the POD kernel and the asterisk indicates a complex conjugate. The i, j subscripts represent the six radial positions.

This estimator was then utilized in the numerical approximation to the integral eigenvalue equation as outlined in § 2.3. In the numeric implementation of this procedure the IMSL package of Fourier transforms was used. More details of the numeric implementation of the POD to the mixing layer are presented in Citriniti (1996).

3. Experiment

3.1. *Facility*

The jet facility for this experiment was the same as that in (I). For this experiment, the exit velocity was $12.5\,\mathrm{m\,s^{-1}}$ which translates to a Reynolds number based on exit diameter of 80 000 for the 9.8 cm diameter nozzle. The turbulence intensity at the jet exit was 0.35% and the boundary layer there was turbulent with an approximate thickness of 0.0012 m. The mean velocity profile was flat to within 0.1%.

The measurements were made at a position 3 diameters downstream of the jet exit, which corresponded approximately to the peak in the radiated noise sources. Because of the high Reynolds number, the shear layer turbulence was fully developed well upstream of this location ($x/d \sim 2$, see I). Since the turbulence is also very nearly self-similar, this location is by no means special, but is representative of the entire shear layer.

For this experiment, the extent of the mixing layer at $x/d = 3$ was defined as $0.15 \leqslant r/d \leqslant 0.80$ where r is the radial position in the flow and d the diameter of the jet at the exit (figure 1). These values were chosen using the results of I such that 95% of the streamwise kinetic energy in the flow was recovered by a grid of extent $0.15 \leqslant r/d \leqslant 0.80$.

3.2. *Spatial measurement-grid design*

3.2.1. *Azimuthal direction*

Since this application of the POD seeks only the most energetic of the structures in the flow field, it is not necessary to resolve all of the azimuthal Fourier modes present in the flow; it is sufficient to recover only those modes which contribute significantly to the streamwise kinetic energy. The results of (I) show that near the potential core, only azimuthal modes 0 and 1 contain significant energy but near the outside of the mixing layer modes up to 15 contain some energy. It is important, however, to ensure that information from the modes that are not of interest is not aliased into those which are of interest by inadequate resolution in space.

For a Fourier, mode-limited field, the number of measurement positions necessary to recover a particular mode must be at least twice the number of modes needed to minimize spatial aliasing, Glauser & George (1992) Thus,

$$N \geqslant 2m + 1,$$

where N is the number of measuring positions and m is the mode number that must be resolved. This is an exact analogy to temporal Fourier mode reconstruction and in this respect the equation above is a spatial Nyquist criterion. Using this criterion, only six measurement positions are necessary to recover the first two important azimuthal Fourier modes at the high-speed side of the mixing layer and at least 32 positions are required at the low-speed side to recover the 15 important modes. Note that data from all these positions are needed simultaneously.

3.2.2. *Radial direction*

The radial direction is of finite extent and strongly inhomogeneous so the Hilbert–Schmidt theory is used in this direction to determine the basis set. Lumley (1970) has shown that the number of modes required to represent the field in an inhomogeneous direction is $L/\mathscr{L}$ where L is the extent of the field and $\mathscr{L}$ is the integral scale. For this experiment $L/\mathscr{L} \approx 3$, consistent with (I) where the POD was performed in the radial direction of the mixing layer and first eigenmode contained 40% of the

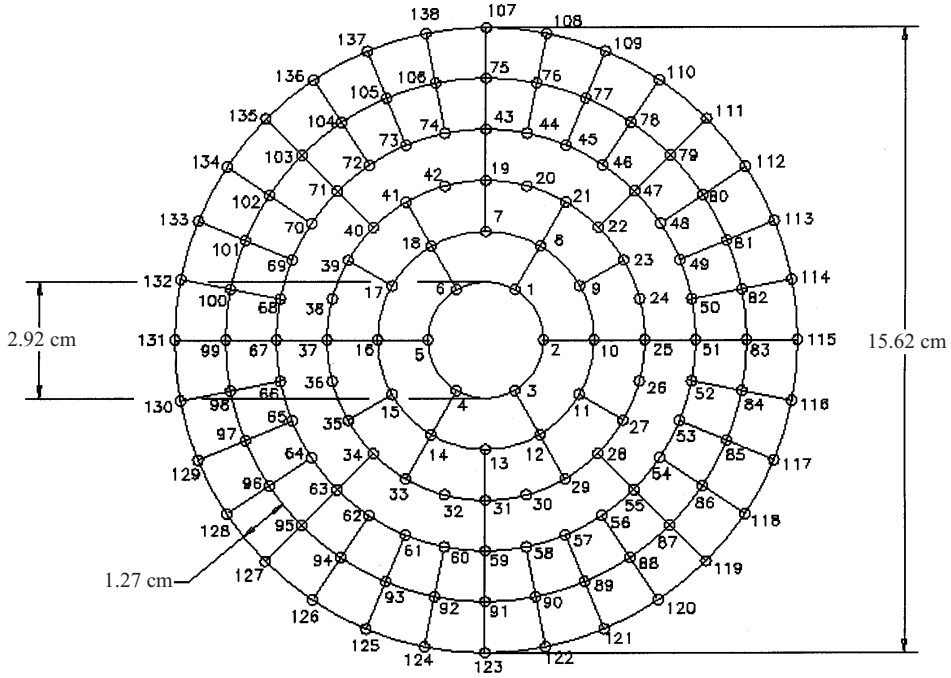

FIGURE 2. Probe array showing the location of 138 probes. Note that each circle represents a single-wire hot-wire probe.

turbulent kinetic energy, with the second and third eigenmodes contributing another 40%. The first three eigenmodes contained 80% of the turbulent kinetic energy and thus three eigenmodes are sufficient to represent the dynamics of the large-scale turbulent structures in the radial direction. This experiment obtained six, of which only the first proved to be important. The POD sampling theorem of Glauser & George (1992) dictates that at least six measurement positions are necessary in the radial direction if the field can be described by only six eigenmodes. This criterion is based on the application of Nyquist diagrams to mode-limited fields in a way similar to that applied in Fourier mode-limited fields.

3.2.3. *Probe array*

The preceding considerations have determined the number of probes needed to resolve the flow field to a sufficient level of accuracy for this application and in figure 2 the results are shown. There are six radial positions, $r/d = 0.15$, 0.28, 0.41, 0.54, 0.67, 0.80, and the azimuthal distribution of probes at these radial positions is, starting at the centre and proceeding outward, 6, 12, 24, 32, 32, 32. Thus there are 138 measurement positions in the mixing layer. Each position in the array contains a single-wire hot-wire anemometer probe.

Flow blockage was of primary concern in the design of the probe array shown in figure 2. With the miniature hot-wire probes used in this experiment the blockage is less than 4% at the point of the probes' main body. The interference at the actual transducer position is considerably less because the probe sensing element extends forward of the probe body by 1.3 cm. The concerns about flow interference downstream of the measurement position due to boundary layer growth and probe cable interference were addressed by utilizing flow visualization techniques to examine

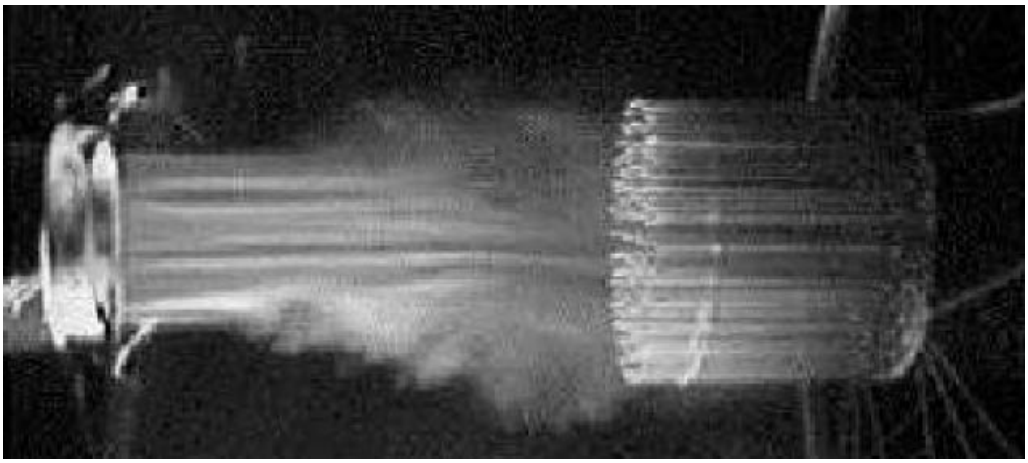

FIGURE 3. Single image taken from the smoke visualization video showing the straight streamlines into the probe front and negligible effect of probe array on the growth of the shear layer.

the flow field before and after the probes were put into position. Using a smoke wire to mark the fluid flow exiting the round jet, a series of videos were recorded to qualitatively asses the effects of the probe array on the formation of the axisymmetric mixing layer. Specifically, we searched for the instances of flow blocking to determine if the probe array impeded flow propagation. Blocking was assumed to exist if bent or irregular streamlines were seen entering the probe array. Over the entire range of operation of the smoke wire (0.5–10 m s^{-1}) no instances of flow blocking were observed on the video. One image, which is representative of the smoke visualization study, is shown in figure 3. These images were compared with others taken with the probe array removed and the streamlines and outer bounds of the mixing layer were similar. For this photo the Reynolds number was reduced to about 8000 in order to accommodate the smoke wire visualization technique in this facility.

3.2.4. *Spatial aliasing reduction*

The difficulty with using a spatial grid is that there will always be some scales which cannot be resolved. Consequently, the information in these unresolvable scales is placed into other modes, i.e. it is spatially aliased. This effect was minimized in two ways: first, by choosing a spatial grid in which nearly all spatial scales which contain energy are resolved; second, by using spatial filtering to reduce information in the unresolvable scales before measurement. The filtering device was a lengthened hot-wire anemometer probe which removed the unwanted spatial scales, thereby acting like spatial filters (Glauser & George 1992). The basic principle is the same as averaging over a time interval in place of low-pass anti-aliasing filters.

A detailed study of the long-sensing-length hot-wire anemometer probe was performed by Citriniti & George (1997). The basic conclusion of this study was that such a probe can be used to reduce spatial aliasing because the hot-wire spatially filters the turbulent scales along the length of its sensing element. Citriniti (1996) has shown that a 1.02 cm wire in a turbulent mixing layer at $x/d = 3$ will reduce 25% of the kinetic energy in azimuthal modes greater than 3 near the potential core and greater than 16 near the outside of the mixing layer. The technique is valid as long as the probe element is not long enough to incur a non-uniform heating distribution.

The hot wires were made of unplated, 12.7 μm tungsten wire (Sigmund-Cohn, Mt.

Vernon, NY) that was welded to in-house probe holders using the DISA 55A12/13 welder and micro-manipulator. The probe holders were made using an injection moulding technique out of Ciba-Geigy Araldite epoxy in which two 0.05 cm steel music wires were used as leads. The l/d ratio for the wires was approximately 800, and they were operated at an overheat ratio of 1.8.

3.3. *Sampling overview*

As shown in (I), it is not necessary to resolve frequencies in the spectrum greater than about 800 Hz to obtain the large-scale structure, so low-pass, anti-aliasing filters were used to filter fluctuations higher than 800 Hz. Accordingly, the sampling rate of the individual anemometers was set at 2048 Hz to satisfy the temporal Nyquist criterion and avoid temporal aliasing. Note that because disturbances are primarily convected in the streamwise direction, temporal variations are really streamwise spatial variations (or mostly so). Hence, temporal filtering is analogous to streamwise filtering, and complements the azimuthal spatial filtering of the long wires described above. Since there is usually strong spatial–temporal coherence of structures in turbulent fields, the combination of the long wires and temporal filtering significantly reduces the possibility of radial aliasing of the turbulent structure.

The record length of each block of data was 1024 samples giving a bandwidth of 2 Hz and a length of 0.5 s. To reduce the variance of the cross-spectra to less than 5%, 290 such blocks were utilized in the statistical analysis. The blocks of data were separated by at least one integral scale to ensure that they each make an independent contribution to the statistical convergence (George, Beuther & Lumley 1978).

The velocity field at all 138 probes was captured at every $\Delta t = 0.5\,\mathrm{s} \div 1024$ samples $= 0.488$ ms. The temporal integral scale in the flow can be estimated from

$$\mathscr{L} = \frac{l}{U_c}, \tag{3.1}$$

where l is the longitudinal integral scale and U_c the convection velocity. The longitudinal integral scale grows at a rate proportional to $0.07x$ in the streamwise, x, direction (Khwaja 1981). Therefore at $x/d = 3$,

$$\mathscr{L} = \frac{0.21d}{0.6U_{cl}}, \tag{3.2}$$

where the convection velocity is assumed to be 60% of the centreline velocity, U_{cl} (Khwaja 1981). For an exit velocity of $12.5\,\mathrm{m\,s^{-1}}$ and a jet diameter of 0.098 m, the integral scale is 0.003 s. In the present experiment, this means there are about six time samples per integral scale. Each of the 290 0.5 s blocks represents approximately 150 integral scales of data.

3.4. *Anemometry*

The anemometers used in this study were also made in-house. The description of them is provided in Citriniti *et al.* (1994) and Citriniti (1996), but the design follows that of Perry (1982) with some modifications to account for the long sensing element of the anti-aliasing, hot-wire probes and to allow for the simultaneous sampling of 138 separate anemometer channels. The characteristics of the 138 channel, simultaneous-sample Buffalo anemometer are comparable to the DISA M systems with respect to frequency response, signal-to-noise ratio and stability (Citriniti *et al.* 1994 and Citriniti 1996). Typical operating frequency response for the anemometers was greater than 12 kHz based on square-wave tests with a test velocity of $10\,\mathrm{m\,s^{-1}}$. Each channel of

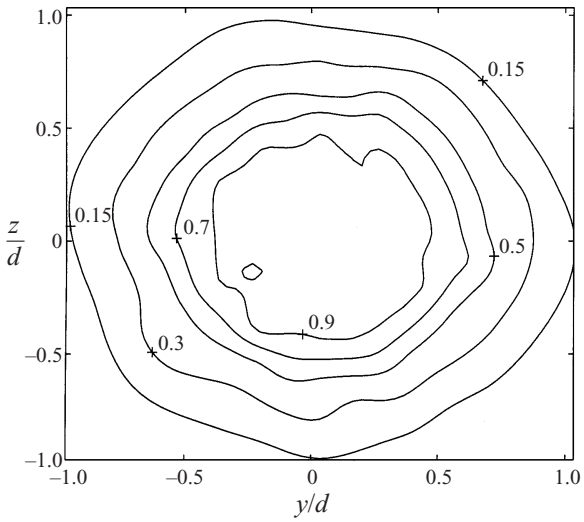

FIGURE 4. Mean velocity contours in the axisymmetric mixing layer normalized by the exit velocity.

anemometry contained its own anti-alias, low-pass, eighth-order Bessel filter with a 48 dB per octave roll-off and a linear phase shift with frequency. The linear phase shift was essential for the simultaneous sampling because a linear phase shift simply causes an identical time delay for all channels and at all frequencies (Citriniti & George 1996).

To ensure that all channels were sampled simultaneously, each channel also had its own sample-and-hold circuit. All channels were strobed at the same instant and then read by the A/D through a 16 channel multiplexer. Since the overall sampling rate was small for each channel (2 kHz), it was possible to connect 16 channels of anemometry to one channel of a high-speed A/D through the multiplexer. The A/D has a maximum sampling rate of 325 kHz which, when divided by the total number of channels, 138, produced a sampling rate of 2350 Hz. This exceeded the Nyquist frequency of the low-pass filtered flow, 1600 Hz.

4. Preliminary results

4.1. *Flow field*

4.1.1. *Mean and RMS statistics*

Contours of mean velocity of the streamwise velocity field using the 138 probe array described in § 3.2.3 are presented in figure 4. These are axisymmetric to within statistical error, thus confirming that an axisymmetric shear layer has been formed and consistent with the observations of (I) in the same facility.

Radial profiles of the mean and RMS velocities normalized by the exit velocity are shown in figure 5. Also shown for comparison are several profiles from similar experiments. The plot shows that much of the velocity field in the mixing layer at $x/d = 3$ is within the bounds of the probe array. The lower RMS values are consistent with the removal of energy by the spatial and temporal filtering. The higher values near the axis are problematic, but are at least partly attributable to electrical noise as discussed in the next section.

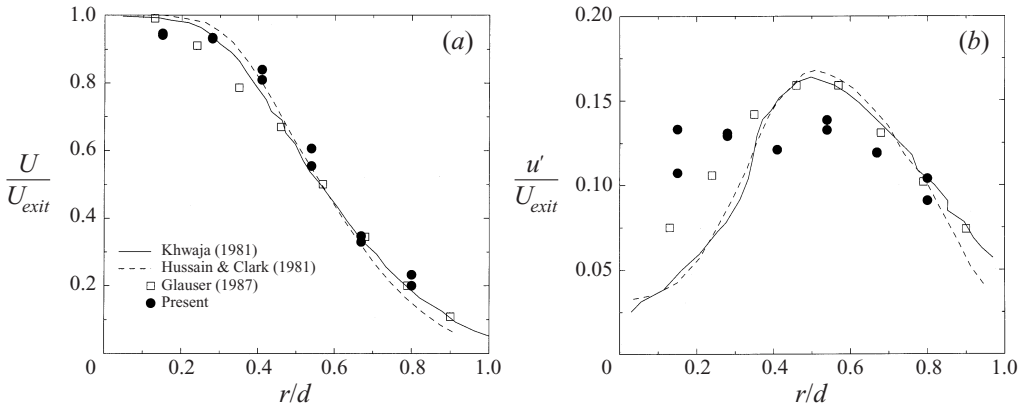

FIGURE 5. Mean and RMS values of the streamwise velocity along a line ($y/d = 0$) in the mixing layer. Comparisons with other experiments. (*a*) Normalized mean velocity, (*b*) normalized RMS velocity.

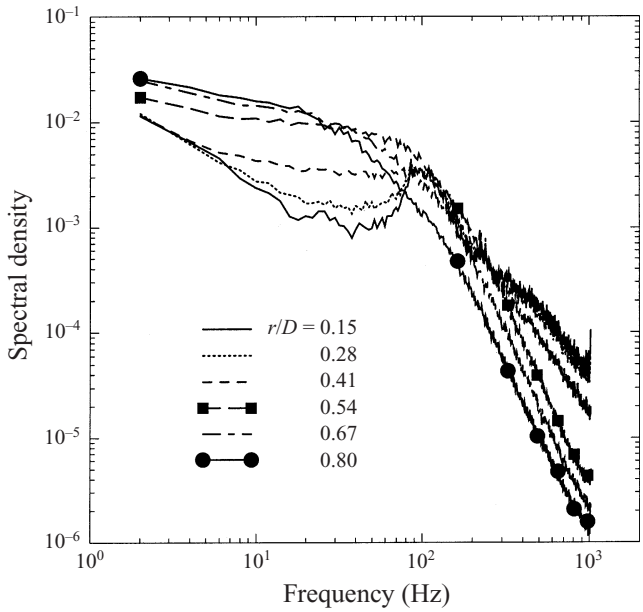

FIGURE 6. Spectra at each of the six radii in the mixing layer.

4.1.2. *Spectra*

The velocity spectra in the mixing layer can be seen in figure 6. The spectra near the high-speed side of the mixing layer, $r/d \leqslant 0.41$, peak away from the origin, which is consistent with (I) and other researchers (cf. Zaman & Hussain 1984 and the references therein). As the mixing layer is traversed radially, the peak in the spectra shifts to the low frequencies shows at least one full decade of $f^{-5/3}$ range denoting high-Reynolds-number turbulent flow. Note that the frequency of the preferred mode in the axisymmetric mixing layer corresponds to the peak in the spectra near the high-speed side in figure 6 (as discussed in I; Zaman & Hussain 1980; and Hussain 1983). The frequency at which this occurs is approximately 100 Hz which corresponds

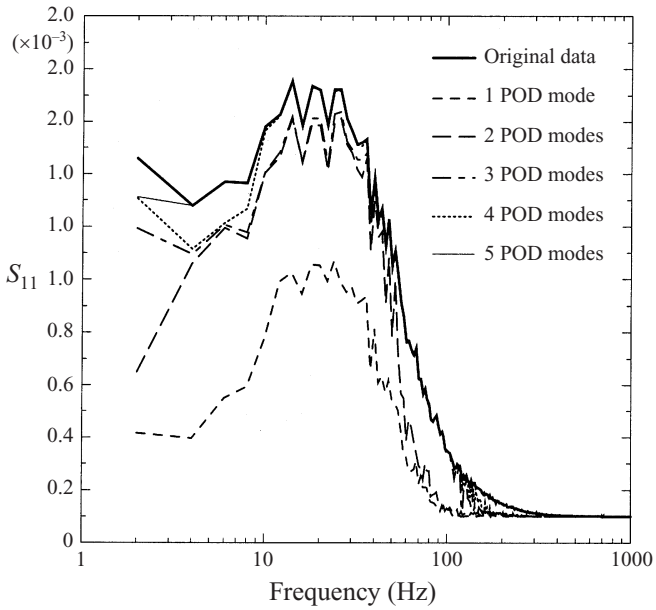

FIGURE 7. POD reconstruction of the spectrum in the mixing layer for the first five POD modes. Spectrum obtained from the hot-wire probe at $r/d = 0.54$.

to a Strouhal number ($St_D = fd/U_{exit}$) of about 0.8, consistent with the presence of the 'jet column' instability mode.

Note that the spectra presented in figure 6 have been post-processed to remove a spike that was discovered in the data from the probes located near the potential core, i.e. $r/d \approx 0.15$. The spike was found to have been added after the anemometers and is uncorrelated with the velocity, therefore it could have no effect on the POD. It could have affected the reconstruction of the original velocity signal, however, and therefore it was removed using a digital filter.

4.2. *Evaluation of the POD decomposition*

4.2.1. *Spectral reconstruction*

The one-dimensional spectrum can be recovered from the POD eigenfunctions as shown by (I):

$$S_{11}(r, m, f) = \sum_{n=1}^{N} \lambda^{(n)} \phi_1^{(n)} \phi_1^{(n)*}. \tag{4.1}$$

A plot of the longitudinal spectrum determined from the instantaneous velocity near the centre of the mixing layer, $r/d = 0.54$, and the POD reconstructed spectrum (from equation (4.1)) for $N = 1, 2, 3, 4, 5$ is shown in figure 7. Clearly, a nearly complete reconstruction of the longitudinal spectrum by the POD is accomplished with only the first few POD modes, consistent with the findings in (I). Integrating under the curves in figure 7 produces the results in table 1 that show a 93% recovery of the original spectrum by the first three POD modes. The POD modes higher than about 3 appear to fill out the reconstruction so that by the fifth POD mode the original spectrum is 99% recovered.

POD modes	Energy percentage (%)
1	68.5
1+2	82.9
1+2+3	93.2
1+2+3+4	96.0
1+2+3+4+5	99.6

TABLE 1. Percentage of energy contained in the first five radial POD modes from a single position in the mixing layer, $r/d = 0.54$.

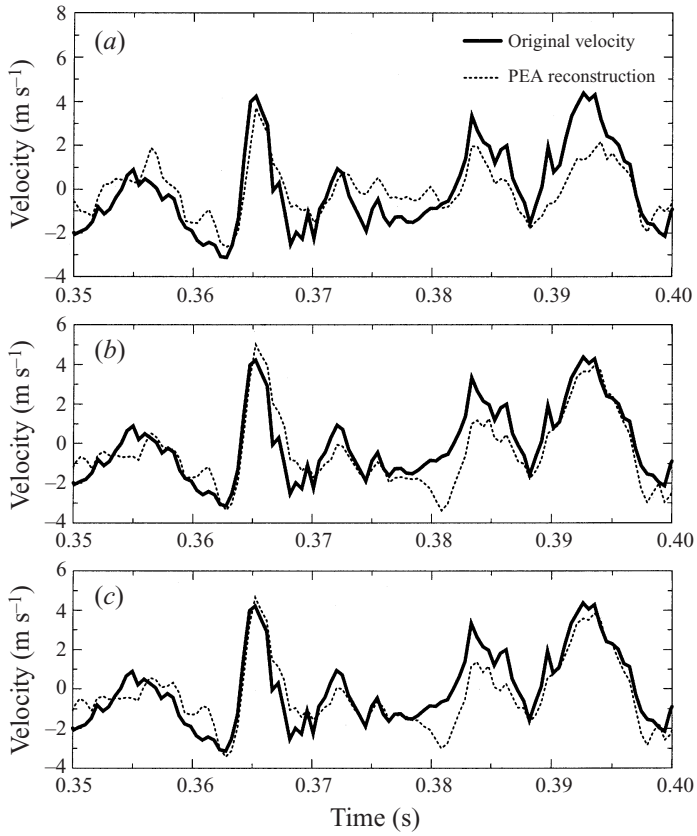

FIGURE 8. POD reconstruction of the instantaneous velocity in a mixing layer for (*a*) the first POD mode, (*b*) the first two POD modes and (*c*) the first three POD modes. A PEA is defined as a Product of the Eigenfunctions and the A, or coefficients, i.e. $a_n\phi_j^n$.

4.2.2. *Instantaneous velocity reconstruction*

The instantaneous velocity at a single position in the mixing layer can be recovered using equation (2.13). The coefficients, $\hat{a}_n(m, f)$, in the expansion are obtained via a projection of the POD eigenfunctions onto the instantaneous signal using equation (2.17). The coefficients can then be used to reconstruct the original signal to see how the various POD modes contribute to the instantaneous events occurring in the layer.

Such a reconstruction is presented in figure 8 where a trace of the original instan-

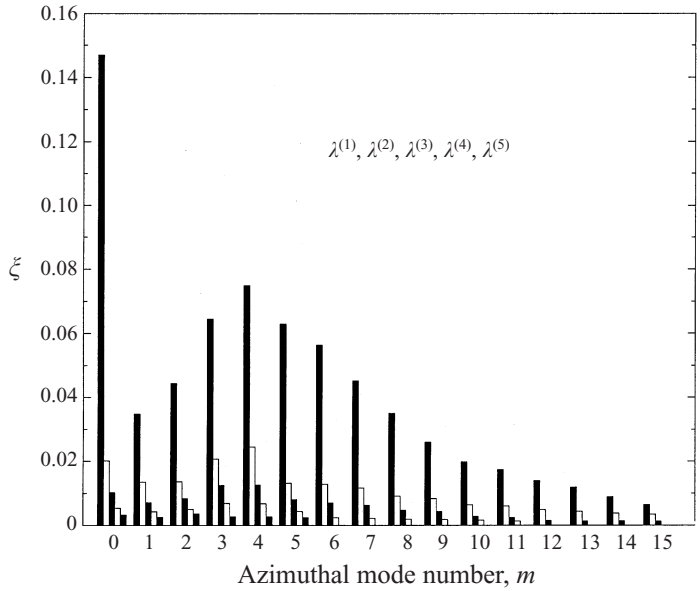

FIGURE 9. Azimuthal-mode energy distribution in the first five POD eigenvalues.

taneous velocity is presented along with the reconstructed signal from the first few POD modes. In part (*a*) of the figure the first radial POD mode is presented. As expected this mode nearly matches the original velocity trace. As more modes are added more of the signal is recovered and with the addition of the third POD mode nearly all of the trace is recovered. Note especially that near the large peaks in the signal the POD reconstruction and the instantaneous velocity signal are nearly indistinguishable. These results are virtually identical to those first presented by Glauser (1987) and illustrate how the POD can be used to efficiently reconstruct statistically stationary and stochastic events in turbulent fields.

5. Results

5.1. *Energy distribution in mixing layer*

In this section, a quantitative measure of the kinetic energy distribution in the first POD mode is presented. Recall from § 2.2 that the total kinetic energy in the flow is equal to the sum of the POD eigenvalues, $\lambda^{(n)}(m, f)$ (equation (2.15)). Since the eigenvalues are already dependent on azimuthal mode number, m, it is useful to look at the distribution of energy for each azimuthal mode within each eigenvalue. Again following (I), a normalized measure of this quantity can be defined by

$$\xi = \frac{\sum_{f} \lambda^{(n)}(m, f)}{\sum_{n} \sum_{m} \sum_{f} \lambda^{(n)}(m, f)}, \tag{5.1}$$

where the denominator is the total streamwise kinetic energy in the flow.

The results of this energy decomposition are presented in figure 9. The first POD mode, represented by $\lambda^{(1)}$, is found to contain nearly 67% of the streamwise kinetic energy in the flow. This agrees well with the value of 68% which was determined in

m	$\lambda^{(1)}$	$\lambda^{(2)}$	$\lambda^{(3)}$	$\lambda^{(4)}$	$\lambda^{(5)}$
0	0.14699	0.20192×10^{-1}	0.10220×10^{-1}	0.53688×10^{-2}	0.31942×10^{-2}
1	0.34754×10^{-1}	0.13498×10^{-1}	0.70824×10^{-2}	0.42293×10^{-2}	0.26098×10^{-2}
2	0.44416×10^{-1}	0.13615×10^{-1}	0.84099×10^{-2}	0.50862×10^{-2}	0.35658×10^{-2}
3	0.64448×10^{-1}	0.20748×10^{-1}	0.12471×10^{-1}	0.68928×10^{-2}	0.27021×10^{-2}
4	0.74914×10^{-1}	0.24522×10^{-1}	0.12653×10^{-1}	0.67353×10^{-2}	0.26648×10^{-2}
5	0.62810×10^{-1}	0.13140×10^{-1}	0.80876×10^{-2}	0.43501×10^{-2}	0.23953×10^{-2}
6	0.56385×10^{-1}	0.12881×10^{-1}	0.69537×10^{-2}	0.24473×10^{-2}	0.57095×10^{-8}
7	0.45118×10^{-1}	0.11649×10^{-1}	0.63502×10^{-2}	0.22333×10^{-2}	0.46394×10^{-8}
8	0.34995×10^{-1}	0.92133×10^{-2}	0.47121×10^{-2}	0.20356×10^{-2}	0.40232×10^{-8}
9	0.25998×10^{-1}	0.84217×10^{-2}	0.43730×10^{-2}	0.19125×10^{-2}	0.25930×10^{-8}
10	0.19795×10^{-1}	0.64195×10^{-2}	0.27688×10^{-2}	0.15937×10^{-2}	0.19117×10^{-8}
11	0.17427×10^{-1}	0.60642×10^{-2}	0.24923×10^{-2}	0.14397×10^{-2}	0.17019×10^{-8}
12	0.14022×10^{-1}	0.50064×10^{-2}	0.15172×10^{-2}	0.14904×10^{-8}	0.74520×10^{-9}
13	0.11901×10^{-1}	0.43410×10^{-2}	0.14233×10^{-2}	0.12537×10^{-8}	0.62686×10^{-9}
14	0.89735×10^{-2}	0.38086×10^{-2}	0.13779×10^{-2}	0.95364×10^{-9}	0.47682×10^{-9}
15	0.64362×10^{-2}	0.34234×10^{-2}	0.13454×10^{-2}	0.67696×10^{-9}	0.33848×10^{-9}
Total	0.66938	0.17695	0.092238	0.044325	0.017132

TABLE 2. Kinetic energy distribution, ξ, in the azimuthal modes for each POD mode.

§4.2.1 at a single position in the mixing layer and again stresses the effectiveness of the POD. Another interesting feature of figure 9 is the energy distribution among azimuthal modes. In the first eigenvalue, there is a definite predominance of the $m = 0$ azimuthal mode with 15% of the total kinetic energy. The next largest azimuthal mode is $m = 4$ with 2.5% and the next three largest modes are 3, 5 and 6. Table 2 lists the numerical values for the kinetic energy distribution and shows that 40% of the kinetic energy is contained in these five azimuthal modes. This implies that although the zero, or ring, mode is dominant, it is also important to consider the effect of these higher azimuthal modes.

5.2. *Global velocity field reconstruction*

5.2.1. *Definition of velocity terms*

The reconstruction of the double Fourier-transformed (frequency and azimuthal modes) velocity field, $\hat{u}_1^{nmf}(r, m, f)$ via the POD basis was shown in §2 to be

$$r^{1/2}\hat{u}_1^{nmf}(r, m, f) = \sum_{n=1}^{N} \hat{a}_n(m, f)\phi_1^n(r, m, f), \tag{5.2}$$

where N is the number of POD modes to sum over and the coefficients, $\hat{a}_n(m, f)$ are in turn given by

$$\hat{a}_n(m, f) = \int r^{1/2}\hat{u}_1^{nmf}(r, m, f)\phi_1^{n*}(r, m, f)\mathrm{d}r. \tag{5.3}$$

The most interesting form of equation (5.2), at least from a visual standpoint, is the inverse Fourier transform in time of $\hat{u}_1^{nmf}$:

$$u_1^{nm}(r, m, t) = \int \mathrm{e}^{\mathrm{i}2\pi f t}\hat{u}_1^{nmf}(r, m, f)\mathrm{d}f \tag{5.4}$$

since it is the time-dependent contribution of each n, m pair. This quantity and various partial sums (i.e. $n = 1, 2, 3\ldots$ and/or $m = 0, 1, 2, 3\ldots$) will be examined in detail, along with its inverse transform in the azimuthal direction, $u^n(r, \theta, t)$, given by

$$u_1^n(r, \theta, t) = \sum_{n=1}^{N} \sum_{m=0}^{M} \mathrm{e}^{-\mathrm{i}m\theta} u_1^{nm}(r, m, t). \tag{5.5}$$

5.2.2. *Presentation techniques*

The magnitude of the streamwise velocity at each of the 138 channels of anemometry is known at $x/d = 3$ for each of the 1024 time steps. Applying the POD to these realizations has produced an orthogonal basis set which, along with the instantaneous coefficients, can be used to reconstruct the velocity field using equation (5.4). The analysis of the previous section has shown that the POD has organized the kinetic energy in the flow so that the first mode contains the most kinetic energy. It is now possible to examine, in a visual sense, the effectiveness of the POD in extracting the structure from the flow. In essence, the POD is being used to filter the small-scale, less-energetic structure from the flow.

The absolute time for each block of data has been indexed by t_p where $1 < t_p < 1024$. The real time can be calculated from the index time, $t = t_p \Delta t$ where $\Delta t = 0.488$ ms. Each of the p 'frames' (i.e. the magnitude of the velocity at each time step, t_p, from all 138 anemometer channels) was imported into a graphics package (Matlab) which mapped the data onto a square grid. The grid density varied for the different presentations but was never less than 40×40. In the following frames, the local mean velocity for each of the probes, determined by integrating over time and ensemble averaging over all 290 blocks, was subtracted before plotting. Temporal evolution of the structure was performed by plotting sequential data sets, i.e. $t_p, p = 413, 414, 415, \ldots$ for instance.

The real power of this approach is best demonstrated by a series of 'videos' produced by temporal sequencing of the 1024 frames. These videos cannot be presented well in a journal article format but they can be accessed via the internet through the Turbulence Research Laboratory home page at SUNY at Buffalo: http://www.eng.buffalo.edu/Research/trl/.

5.2.3. *Extraction of large-scale structure*

The POD reconstructed velocity field can be compared to the original velocity to see if it is truly extracting structure from the seemingly random flow. Figure 10 shows surface mesh plots of the magnitude of the streamwise velocity at a single time step, $t_p = 413$, obtained directly from the hot-wire probes and from the corresponding POD reconstruction using only the first radial POD mode (i.e. $N = 1$ in equation (5.5)). Part (a) of this figure shows the original velocity which contains many peaks. It is difficult to determine which peaks are due to spatially coherent structures and which are due to small-scale perturbations. In part (b) of this figure, the POD reconstruction is shown in which only the first radial POD mode and all azimuthal modes are included (i.e. $N = 1$ and $m = 0$–15 in equation (5.4)). The POD modes not used have in effect filtered out many of the small-scale perturbations while those used have retained the features representative of the spatially coherent structure. Since the higher azimuthal modes, $m \geqslant 7$, do not contribute significantly to the spatially coherent structures, they can also be removed as is done in figure 10(c). This is accomplished by setting the appropriate azimuthal Fourier modes to zero in equation (5.4) and then inverse

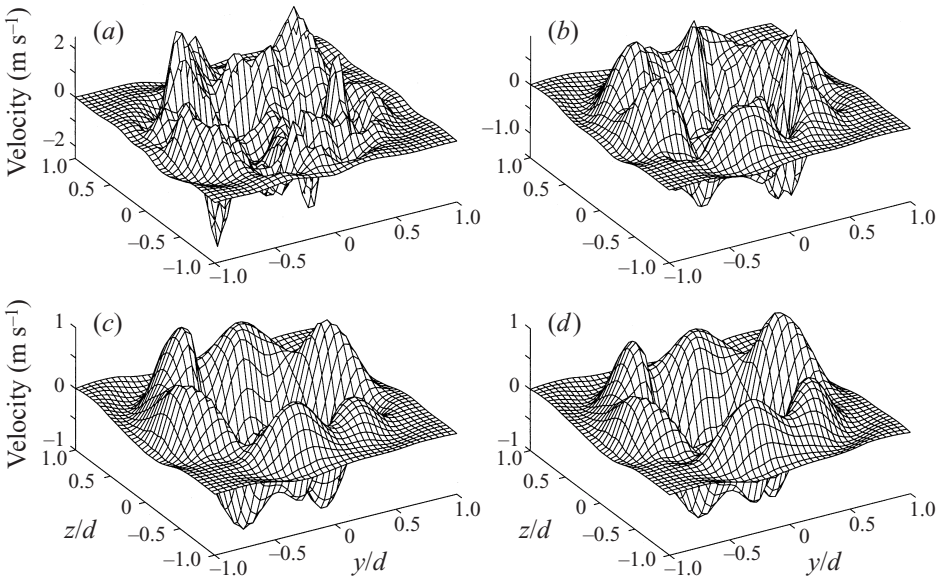

FIGURE 10. Surface mesh of streamwise velocity field at $x/d = 3$ with $t_p = 413$ from (*a*) the original hot-wire measurements and the POD reconstruction (equation (5.4)) using only the first POD mode and including (*b*) all azimuthal modes, i.e. $m = 0 - 15$ (*c*) $m = 0 - 6$ and (*d*) $m = 0, 3, 4, 5, 6$.

Fourier transforming in time to get the temporal reconstructed velocity in equation (5.5).

Further refinement of the large-scale structure is accomplished by removing other unimportant azimuthal modes from the POD reconstruction. The results of § 5.1 indicated that much of the energy in the flow was contained in azimuthal modes 0, 3, 4, 5 and 6 (figure 9). If only these modes are included in the representation, a further filtering of the small-scale structure can be accomplished, figure 10(*c*). It should be noted that this decision is not made arbitrarily since the POD has provided the information that led to the exclusion of these unimportant modes, namely through figure 9. This is in contrast to conditional sampling approaches where the basic structure is defined by threshold criteria which are determined by observation rather than by the statistical nature of the flow.

This process of reducing the information in the reconstruction can obviously continue until all that remains is the mean velocity. However, figure 10(*d*) shows that the first POD mode including the azimuthal modes 0, 3, 4, 5 and 6 sufficiently recovers the large-scale structure. Thus the POD has reduced a very large dimensional problem to one involving only five parameters while retaining all of the essential features of the large-scale motion.

5.3. *Large-scale structure dynamics*

To illustrate the dynamics of the structure in the mixing layer, a sequence of frames will be presented which show the interaction and shape of the large-scale structure typifying the events in the layer at $x/d = 3$. The block number for this presentation is 234 (out of 300) and the time index begins at $t_p = 413$ and continues to $t_p = 433$ which corresponds to a real time span of 9.765 ms. Only the first radial POD mode is used to reconstruct the magnitude of the streamwise velocity, including only azimuthal

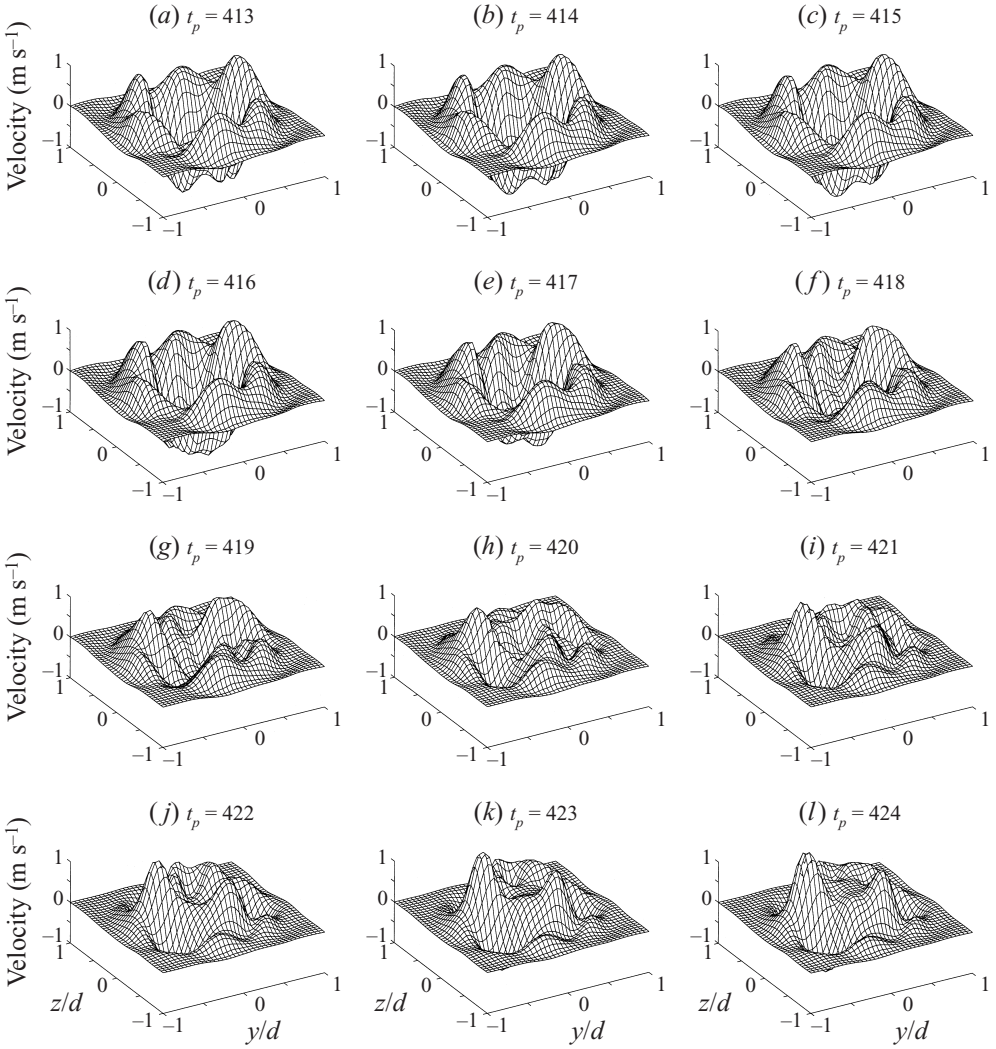

FIGURE 11 (*a–l*). For caption see facing page.

modes 0, 3, 4, 5 and 6. In the following discussion, the emphasis will be on two main mechanisms for large-scale structure evolution in the mixing layer.

5.3.1. *Bursting event of an azimuthally coherent structure*

The first presentation will utilize the three-dimensional surface projection technique described in § 5.2.2. An especially interesting sequence of frames from one section of a reconstructed velocity 'movie' is presented in sequential order in figure 11. The most prominent feature is the volcano-like event which appears in its fullest form in figure 11(*k*). The shape of the structure causing the volcano cannot be determined precisely by the streamwise-only measurements made here, but it appears obvious that this is one of the azimuthally coherent vortex rings (or the azimuthally perturbed remnants of a ring) observed in many visualization and conditional sampling experiments (e.g. the pictures by Wille and Michalke in Van Dyke 1982 and Zaman & Hussain 1984), and also the proposed model of the mixing layer dynamics in (I). The

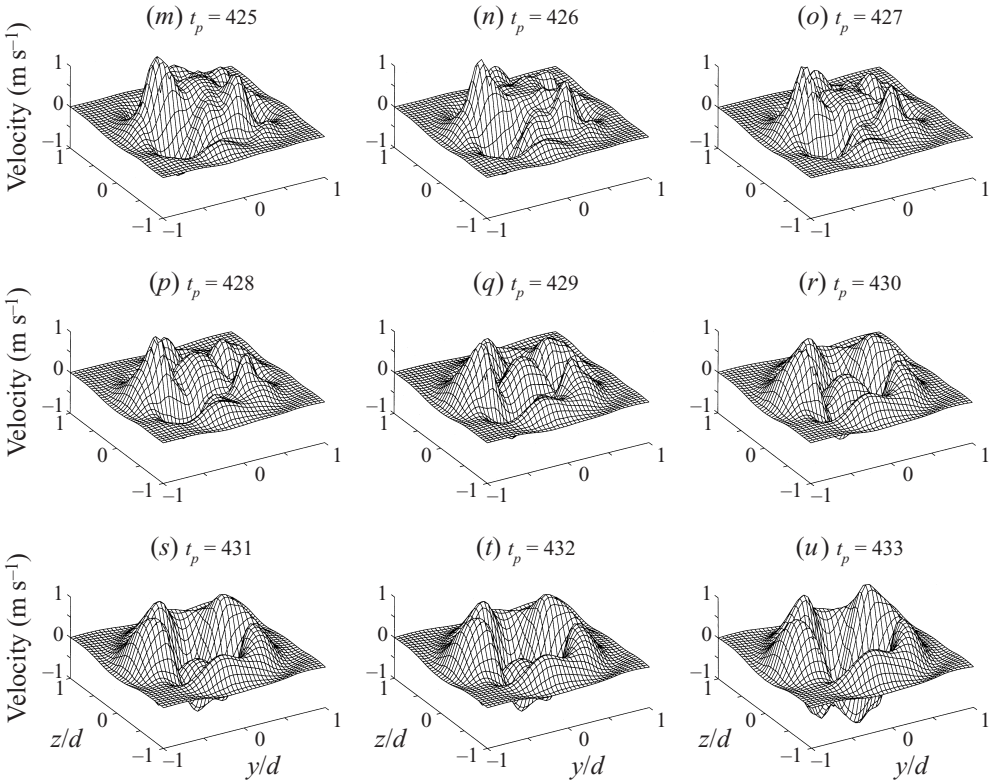

FIGURE 11. Surface mesh of streamwise velocity field at $x/d = 3$ using only the first POD mode and including azimuthal modes $m = 0, 3, 4, 5, 6$. The time indices are indicated in the individual captions.

azimuthally coherent, but short-lived, eruption forces high-velocity fluid through its centre causing a peak in the streamwise velocity near the potential core and extending in the layer to $r/d \approx 0.5$ thus producing the volcano-like structure in figure 11(*j–m*). Simultaneously, the velocity is driven below the mean outside the half-width of the mixing layer. Note that at this diameter, the 'ring' does not appear circular but rather has been perturbed into a multi-lobed structure. This point will be discussed further in a later section where the shape of structure will be presented in a more obvious manner.

5.3.2. *Dynamics of streamwise vortex pairs*

The appearance of the volcano event in figure 11(*k*) is preceded in time by a six-mode structure (or structures) which has a large impact on the streamwise component of the velocity field as shown in figure 11(*a–e*). A possible explanation for these regions of increased streamwise velocity could be the outward advection of high-velocity, potential core fluid by counter-rotating streamwise vortex pairs. (These have been described in Liepmann 1991, Liepmann & Gharib 1992 and Martin & Meiburg 1991 for the axisymmetric layer and Bernal & Roshko 1986, Corcos & Lin 1984 and Metcalfe *et al.* 1987 for the plane mixing layer.) The streamwise vortex pairs advect high-velocity fluid from the potential core (causing the six-mode peaks in the velocity field in figure 11*a*) and also advect slow-moving fluid from the low-speed side of the layer to the potential core. The 'valleys' corresponding to the reduced streamwise

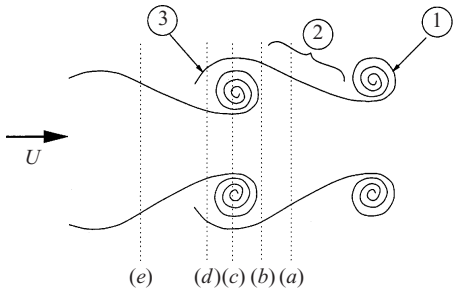

FIGURE 12. Sketch of coherent structure interaction with (1) the azimuthally coherent ring, (2) the braid region and (3) the streamwise component of the large-scale motion.

velocity are not easily visible in figure 11 but will become more evident in the next section. Note that the six-mode peaks near the outside of the layer tend to remain in the measurement plane for long periods of time, most likely because they are on the outside of the mixing layer where the mean advection velocity is very low.

Subsequent to figure 11(*a*), the streamwise velocity peaks in the outer portion of the layer increase for a short time. However, by figure 11(*e*), which is about 2 ms after figure 11(*a*), the peaks begin to reduce in magnitude as the bursting event begins to enter the measurement grid. In frames (*n*–*p*) the streamwise structures are pushed to the outside of the layer and coexist with the coherent 'ring' which passes through the $x/d = 3$ plane by figure 11(*o*). A new set of ribs arrives with the azimuthal ring in figure 11(*p*). As the ring passes the measurement plane and its effect decreases, the streamwise vortices appear to gain strength due to the large extensional strain between the azimuthal 'rings', thereby increasing their influence on the velocity field (Martin & Meiburg 1991). One life cycle of the large-scale structure ends in figure 11(*u*) when the characteristic multi-peak streamwise velocity profile returns. The length of time for one life cycle is typically 10 ms.

It is interesting to note the modal structure at the beginning of the cycle, figure 11(*a*), contains a 6-mode symmetry but by the end of the cycle has only a 5-mode symmetry. The authors have witnessed 3-, 5- and 6-mode structure in the movies with the 5-mode structure being the most prevalent. These observations support the conclusions of the POD energy decomposition presented in § 5.1 and in (I) that the important azimuthal modes are 0, 3, 4, 5 and 6.

5.4. *Interaction of large-scale structure in the mixing layer*

In the following analysis, a different presentation technique, the plane projection method, will be used to illustrate in more detail the large-scale structure dynamics. The plane projection method maps the streamwise velocity of all 138 probes onto a two-dimensional plane, i.e. an (r, θ) plane at $x/d = 3$, with a 60×60 grid. The magnitude of the velocity is represented by a range of colours. In the format of a journal paper it is not possible to present all of the full-colour frames but a series of images is presented to give a view of the structure in the layer. The frames presented below correspond roughly to the time index frames of the three-dimensional surface projection of § 5.3.1 and so the same structural events are presented. The red areas in the images represent regions of the plane where the streamwise velocity is greater than the local mean velocity and regions of blue colour indicate a velocity less than the local mean.

Figure 13(*a*) shows a typical two-dimensional projection in which the distinct six-mode structure of alternating high-momentum (red) and low-momentum (blue) fluid

occurs near the middle of the mixing layer, $r/d \approx 0.5$. The position of the frame in figure 13(*a*) relative to the emergence of the azimuthal ring structure (discussed in § 5.3.1) is sketched as (*a*) in figure 12. This provides a rough guide to the temporal sequencing of events displayed in figure 13(*a–u*). The dashed lines in figure 12 represents the position of the measurement grid as the spatially developing rings and streamwise structures move past.

The plus and minus signs which have been added to the first frame of figure 13 are meant to indicate the suspected position of the counter-rotating streamwise vortex centres. Positive vorticity would mean that the induced velocity field would rotate counterclockwise, centred on the plus sign. Note that the counter-rotating nature of the vortices creates alternating positive and negative radial fluid advection patterns. For example, to the right of a (+) vortex the induced velocity field would advect fluid from the potential core to the outside of the layer, i.e. a positive mean radial velocity. The (−) vortex to the right of the (+) vortex would add to this advection velocity since its induced velocity field is also directed in the positive radial direction. The combined effect would create an ejection of high-streamwise-momentum fluid from the core to the outside of the mixing layer, in essence a side jet. The induced velocity field to the left of this (+) vortex would be directed toward the jet centreline and the induced velocity field of the (−) vortex to its left would add to this effect. In this case the combination would advect low-streamwise-momentum fluid from the outside of the layer to the potential core.

The hypothetical advection pattern described in the previous section is consistent with what is found in the layer. In figure 13(*a–h*), the streamwise vortices advect the regions of high streamwise velocity toward the potential core while moving fluid with low velocity toward the outside of the layer. This process continues until figure 13(*i*) where it appears that the induced velocity field of the 'ring' structure begins to enter the $x/d = 3$ plane.

In figures 13(*i*) and 13(*j*) the strength of the streamwise vortex pairs begins to decrease and there is a definite increase in the overall velocity of the fluid near the potential core. Figures 13(*l*) and 13(*n*) show the effect of the ring passing through the measurement plane; the fluid near the middle of the jet is accelerated due to the induced velocity field of the coherent ring and the streamwise vortex pairs are advected toward the outside of the layer. The coherent structure causing the star-shaped pocket of high-momentum fluid in figure 13(*l–n*) is definitely not circular. Nonetheless, because of its ability to accelerate fluid through its core while advecting the streamwise vortices to the outside of the layer, it is natural to consider this volcano-like eruption to be the consequence of an axisymmetric ring, or, more appropriately, the azimuthally perturbed remnant of a ring. As these figures show, it is convected by the flow and its immediate effects on the flow are very short lived (only about 20% of the life-cycle time span). These are very similar to the vortex rings previously suggested to play an important part in the entrainment and growth in this layer (Yule 1978 and Lau & Fisher 1975)

It is interesting to notice that in figure 13(*j*) there is a definite 4-mode structure appearing near the centre of the mixing layer. This location of the $m = 4$ structure explains the dominance of the fourth mode in the decomposition of the kinetic energy in the flow (§ 5.1 and I), since it is associated with the portion of the layer containing the highest velocities and therefore contains the most kinetic energy.

Figure 13(*l*) marks the centre of the passing coherent ring (corresponding to (*c*) in figure 12). As the ring passes the measurement plane, a new set of ribs emerges. These structures have been wound into the core of the ring by its induced velocity

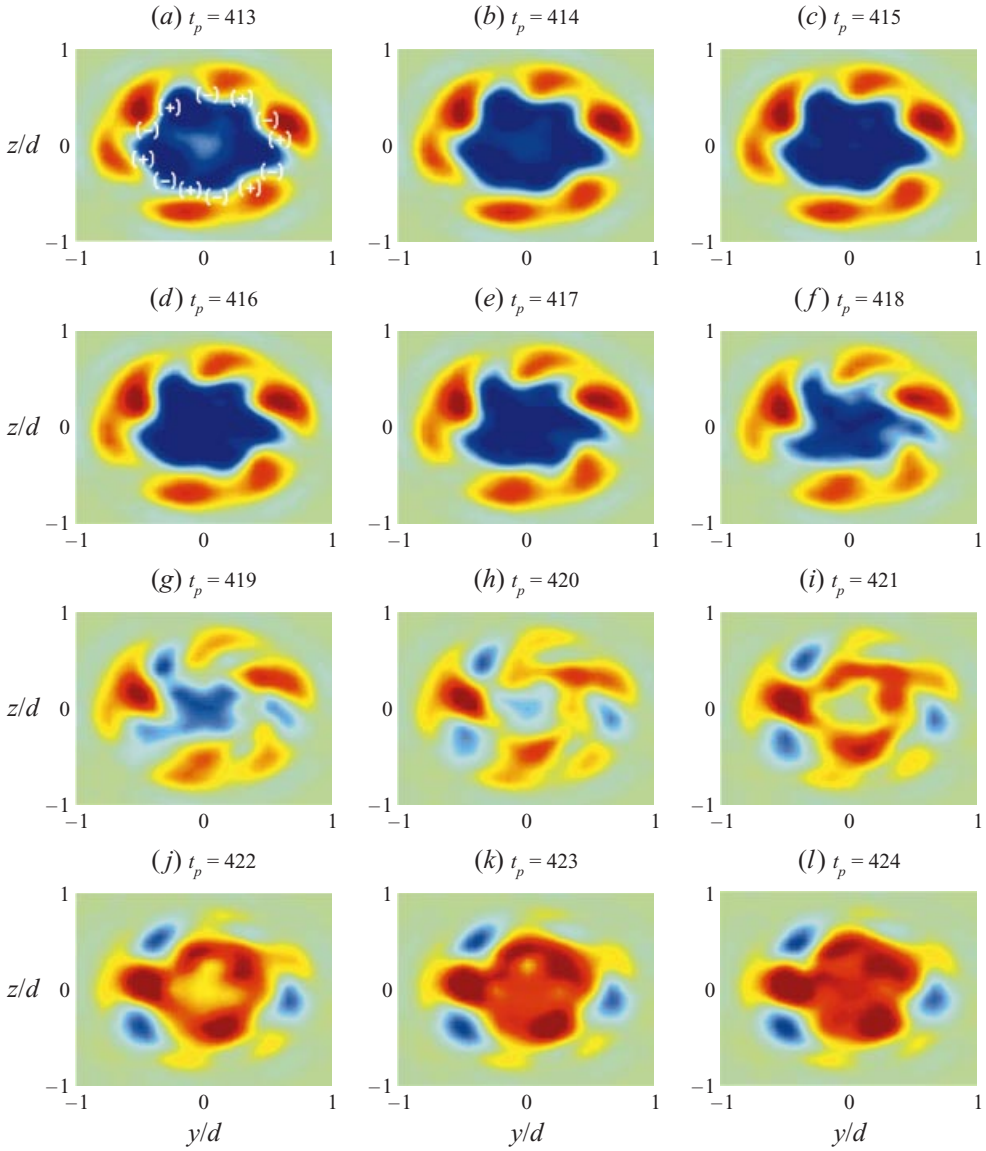

FIGURE 13 (*a–l*). For caption see facing page.

field and in figure 13(*n*) two concentric sets of streamwise vortex pairs are evident. This situation is represented by (*d*) in figure 12. The outer set of streamwise vortices is quickly destroyed by the high shear gradient in the mean field and by figure 13(*r*) there is only one set apparent. The cycle of large-scale structure interaction completes at approximately figure 13(*u*) which corresponds roughly to (*e*) in figure 12. The interaction of the rings and streamwise structure described above varies slightly from cycle to cycle, but the basic mechanism is the same.

5.5. *Large-scale structure properties*

Some interesting observations can be drawn with respect to the azimuthally coherent ring which appears near the potential core. The length of time for the volcano (or

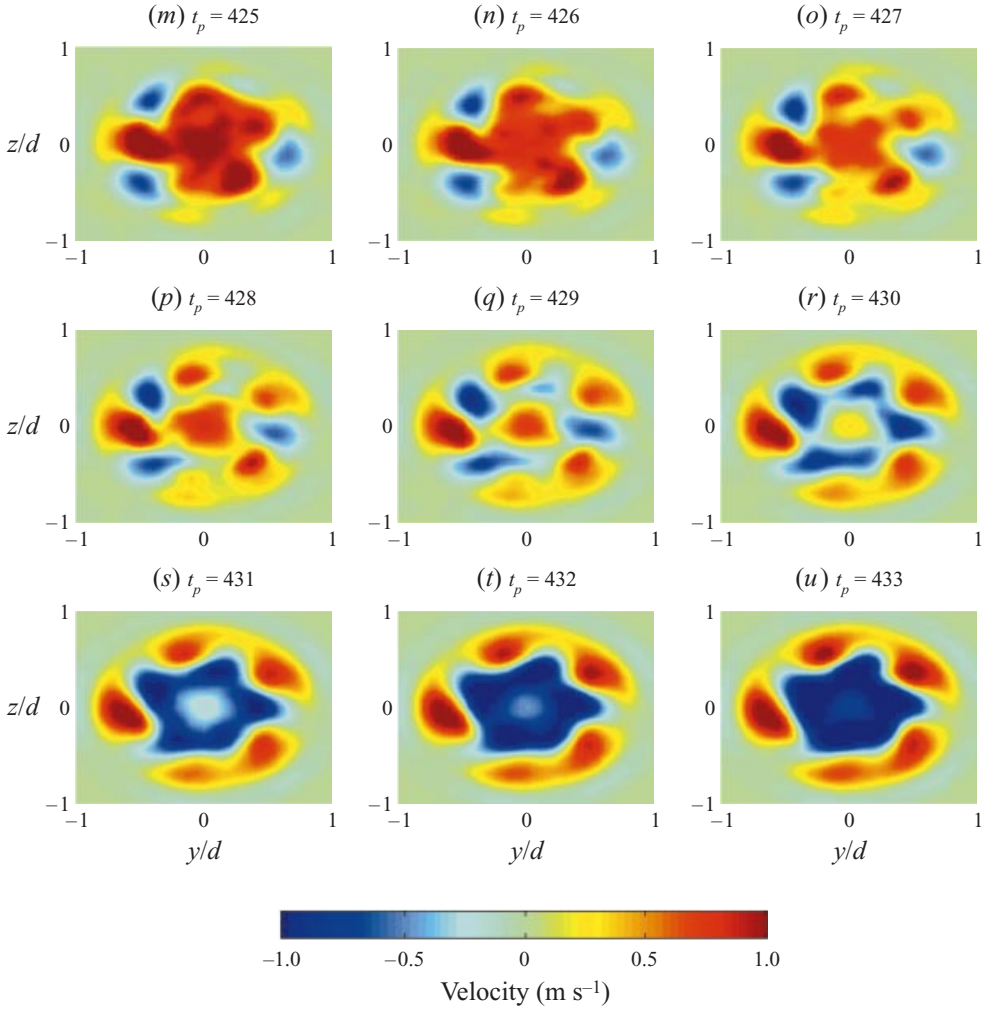

FIGURE 13. Surface mesh plot of the streamwise velocity field with the mean subtracted at $x/d = 3$ using only the first radial POD mode and including azimuthal modes $m = 0, 3, 4, 5, 6$. The time indices are indicated in the individual captions. The colour scale for the velocity is given in the last frame.

ring) to pass through the measurement plane can be estimated to be about 10 frames long, frames 13(*g*–*p*), or about 5 ms. Note that the actual passage time of the ring is smaller than this because the induced velocity field extends well beyond the vorticity. However, from the two-dimensional plane projections in the previous section it is possible to define the ring proper as entering the measurement plane at frame 421, figure 13(*i*), and exiting the plane at frame 426, figure 13(*n*). This corresponds to a residence time of 2.9 ms. If the azimuthal ring is assumed circular in cross-section, its diameter can be estimated from figure 13(*j*) to be about 2.1 cm. Then, the convection velocity of the ring can be calculated:

$$U_c = \frac{d}{\Delta t} = \frac{0.021}{0.0029} = 7.2\,\mathrm{m\,s^{-1}} \tag{5.6}$$

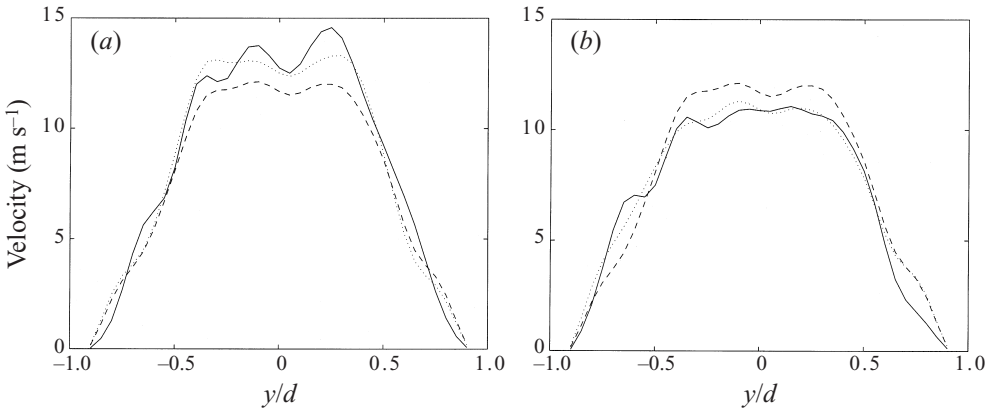

FIGURE 14. Plot of instantaneous velocity profile compared with block mean: —, original velocity from hot-wire probes; ···, POD reconstructed velocity with $N = 1$, $m = 0, 3, 4, 5, 6$; – – –, block mean velocity. (*a*) $t_n = 423$, (*b*) $t_n = 433$.

which is identical to the velocity obtained using 60% of the centreline velocity ($12\,\mathrm{m\,s^{-1}}$ at $x/d = 3$).

It is also interesting to note that the passage time of these coherent 'ring' structures corresponds to the Strouhal frequency in this flow (≈ 0.8). That is, one ring passes the measurement plane ($x/d = 3$), on average, every 20 frames or every $20 \times 0.488 \times 10^{-3} = 9.76 \times 10^{-3}$ s. The frequency of this passage is $1/\Delta t = 102$ Hz. This corresponds to a Strouhal frequency based on exit diameter of

$$S_{td} = \frac{f d}{U_{cl}} = \frac{102(0.098)}{12} = 0.8. \tag{5.7}$$

Obviously the volcano event observed here is the same as has been used for conditional sampling by many investigators (e.g. Hussain 1986). As suspected by them, but never proven (since they were only able to sample radial slices of the flow instead of the cross-section available here), it is indeed a *spatially coherent burst covering most of the flow field*. This is quite unlike Townsend's picture of large turbulent eddies which are associated with slower motions nor is it anything like the normal picture of energetic eddies the size of the integral scale. In fact, paradoxically, the largest spatial structure is also the most energetic and the shortest lived.

5.6. *Mean flow perturbations*

An interesting question which often arises in stability and dynamical system analyses of turbulence is: what is the base flow for turbulent shear layers? Generally it has been assumed that the base flow more or less corresponds to the mean flow (e.g. Crow & Champagne 1971). This presumes that the mean flow is really present and the fluctuations are perturbations around it. It is possible, however, that the mean flow never exists at any instant in time, but is simply the average of the events which transpire. For this one case at least, it is possible to show that the mean flow is indeed usually present. To see this a slice of the flow field in its POD reconstructed and original form is presented in figure 14 where the magnitude of the instantaneous streamwise velocity at $z = 0$ is shown. In figure 14(*a*) the azimuthally coherent 'ring' is passing through the measurement grid and the velocity near the centre of the mixing layer is obviously being accelerated above the mean. The POD reconstructed velocity is also seen to follow the original velocity. After the ring has passed the measurement

plane, the instantaneous and POD reconstructed fluid velocity is found to be less than the mean, indicating that low-momentum fluid has been advected toward the potential core, as seen in figure 14(*b*). Further influence of the streamwise vortices is shown in figure 14(*b*) where a small region of high-momentum fluid is advected toward the outside of the mixing layer near $y/d = -0.6$. Note that the timing of these events is consistent with the modified two-ring model where the streamwise vortices are found in the region between the rings.

It is apparent from this figure (and even more so from movies showing many such images) that there is indeed a 'base' profile for this flow and it is the mean velocity profile. The figure clearly shows a perturbation of the instantaneous velocity about the mean profile. The passage of a ring structure corresponds to the centre of the profile growing at the expense of the outer region, while during the braid region the opposite effect is seen. It is also interesting to note that the position where the mean and instantaneous profiles cross occurs, on average, at about $7\,\mathrm{m\,s^{-1}}$ which is the convection velocity of the ring structure (§ 5.5). This would tend to explain the success of linear stability analyses (Michalke 1965). It also gives credence to the use of linearized, POD decomposed Navier–Stokes equations as suggested by Lumley (1967) who noted their relation to the Orr–Sommerfeld equation.

6. Summary and discussion

The Proper Orthogonal Decomposition has been shown to be a useful tool in large-scale turbulent structure identification. The ability of the POD to extract structure objectively has been shown by visual and numerical means. Because of the rigour with which the POD defines the structure, the dynamics of these structures can now be studied.

It is possible to define a life cycle of the large-scale structure dynamics in the mixing layer at $x/d = 3$ by using the POD to filter the small-scale turbulent fluctuations which obscure the view of the large structures. The most obvious event in the life of the coherent structures is the volcano-like bursting event associated with the passage of an azimuthally coherent structure, or 'ring', near the potential core. The volcano (or 'ring') is typically not round but contains higher modes as well. These 'rings' eject high-streamwise-momentum fluid through their core, creating the aforementioned bursting event. The induced velocity field between successive rings creates a high strain field that seems to play an important role in the evolution of counter-rotating streamwise vortex pairs, or ribs. The ribs are found throughout the large-scale-structure life cycle, so they both coexist with the ring structure and are strengthened in the strain region between successive rings. The ribs seem to be an integral part of the entrainment process in the mixing layer as they advect high-velocity fluid directly from the potential core to the outside part of the layer and low-velocity fluid from the outside directly to the potential core. This process also involves the induced velocity field of the ring structure, so the entrainment process is therefore a result of the induced velocity field of both.

In the high-strain region between the rings, the ribs become elongated by the strain field. Also, a portion of the structure is wound into the core of a following ring while some escapes and is pushed to the outside of the mixing layer. The radial gradient of the mean velocity field near the outside of the layer causes the ribs to stretch and become more compact in a process that may signal an energy transfer from larger to smaller structures.

The physical production mechanism for the streamwise vortex pairs cannot be

determined from this data set but two possible explanations are considered. First, the vorticity may be the remnants of an outer ring which has been driven unstable by the action of a rearward ring which has been advected through its core in a classical leap-frog interaction. The outer ring would be susceptible to instability mechanisms because of its reduced core size (Widnall & Sullivan 1973) and would typically adopt a multi-lobed, sinuous core shape. The mean velocity field would tend to advect the portions of the multi-lobed ring which are closer to the potential core at a faster rate than those further out in the flow and thus stretch and turn the vorticity into the streamwise direction, i.e. by a 'global induction' mechanism (Martin & Meiburg 1991). The azimuthally perturbed outer vortex ring is strained due to the mean velocity field producing the counter-rotating streamwise vorticity pairs described above. This mechanism is consistent with the two-ring model of the mixing layer dynamics suggested in (I) and Glauser (1987) and also affirmed by Lim (1997). This model not only describes many of the physical interactions witnessed in the figures presented in this report, but also describes an instability mechanism for the destruction of the large-scale structure which must occur before the beginning of the self-similar region of the layer.

A second generation mechanism could be the creation of streamwise vorticity in the so-called 'braid' region between azimuthally coherent rings. In this hypothesis, a global instability mechanism would be amplified by the strong extensional strain field existing between two successive rings in the mixing layer (D. Ewing, private communication). The layer has been shown to be susceptible to instability mechanisms in this braid region which result in the production of counter-rotating streamwise vortex pairs as demonstrated by Martin & Meiburg (1991). The coherent ring near the potential core is produced by natural instabilities in the shear layer downstream of the nozzle lip. What is missing in this hypothesis is an actual instability mechanism for the production of streamwise vorticity and the subsequent breakdown to small-scale turbulence.

Whatever the generation mechanism, the impact of the streamwise structure on the dynamical processes of the mixing layer is quite significant. The velocity field induced by the streamwise structure directly injects fluid into and out of the potential core. This suggests that the impact of ribs on the entrainment field is similar to that of the azimuthal ring structure. In this regard, the streamwise eddies are much more influential than their more passive counterparts in the plane mixing layer (see Corcos & Lin 1984). This may be one reason why stimulation of the $m = 5$ and $m = 6$ modes in the mixing layer produces increased mixing in the jet (Zheng & Glauser 1991; Corke, Glauser & Berkooz 1994; and Citriniti 1997). By stimulating these higher azimuthal modes, one is directly adding energy to the rib structures and increasing their ability to entrain fluid.

The videos produced via sequential presentation of the full field measurements have shown that the azimuthal distribution of the streamwise structure in the jet is not completely described by an $m = 5$ structure. Its structure can exhibit 3-mode, 5-mode or even 6-mode tendencies. Also, the $m = 4$ mode is typically seen near the potential core in the mixing layer, which together with the high velocities of the fluid in this region explains why the $m = 4$ mode makes such a large contribution to both the streamwise kinetic energy in the flow (figure 9) and the total kinetic energy in the flow (I).

This work was completed with the support of the National Science Foundation grant number CTS-9102863 and AFOSR grant number F4920-98-1-0143. The authors

are indebted to the many people who assisted with the completion of this work. Special thanks to D. Ewing for many helpful discussions on the theory and S. Woodward whose assistance in the experimental aspect of the work was indispensable. Thanks also to K. Taulbee who designed the anemometers and to the ECS staff at SUNY Buffalo for their computational assistance. Thanks also to Chalmers University of Technology in Gothenburg, Sweden where much of the data processing and graphical presentation was performed. Finally a special acknowledgement to D. Jung and S. Gamard for their help in checking thoroughly the POD analysis in chapter 2 and correcting the present manuscript.

REFERENCES

Bernal, L. P. & Roshko, A. 1986 Streamwise vortex structure in plane mixing layers. *J. Fluid Mech.* **170**, 499–525.

Breidenthal, R. 1981 Structure in turbulent mixing layers and wakes using a chemical reaction. *J. Fluid Mech.* **109**, 1–24.

Browand, F. K. & Weidman, P. D. 1976 Large scales in the developing mixing layer. *J. Fluid Mech.* **76**, 127–144.

Citriniti, J. H. 1996 Experimental investigation into the dynamics of the axisymmetric mixing layer utilizing the proper orthogonal decomposition. PhD thesis, State University of New York at Buffalo.

Citriniti, J. H. 1997 Aximuthal mode interaction in an unforced high Reynolds-number axisymmetric shear layer. In *Proc. AIAA Fourth Shear Flow Control Conference, Snowmass, CO*.

Citriniti, J. H. & George, W. K. 1996 Experimental investigation into the dynamics of the axisymmetric jet mixing layer. In *Turbulence, Heat and Mass Transfer, 1* (ed. K. Hanjalic & J. C. F. Pereira). Begell House.

Citriniti, J. H. & George, W. K. 1997 The reduction of spatial aliasing by long hot-wire anemometer probes. *Exps. Fluids* **23**, 217–224.

Citriniti, J. H., Taulbee, K. D., Woodward, S. H. & George, W. K. 1994 Design of multiple channel hot-wire anemometers. In *Fluid Measurement and Instrumentation 1994*. ASME FED, Vol. 183, pp. 67–73.

Corcos, G. M. & Lin, S. J. 1984 The mixing layer: deterministic models of a turbulent flow. Part 2. The origin of the three-dimensional motion. *J. Fluid Mech.* **139**, 67–95.

Corcos & Sherman, F. S. 1984 The mixing layer: deterministic models of a turbulent flow. Part 1. Introduction and the two-dimensional flow. *J. Fluid Mech.* **139**, 29–65.

Corke, T. C., Glauser, M. N. & Berkooz, G. 1994 Utilizing low-dimensional dynamical systems models to guide control experiments. In *Appl. Mech. Rev.* (ed. A. S. Kobayashi), Vol. 47, no. 6, part 2, pp. s132–s138.

Crow, S. C. & Champagne, F. H. 1971 Orderly structure in jet turbulence. *J. Fluid Mech.* **48**, 547–591.

George, W. K. 1988 Insight into the dynamics of coherent structures from a proper orthogonal decomposition. In *Symposium on Near Wall Turbulence, Dubrovnik, Yugoslavia*.

George, W. K., Beuther, P. D. & Lumley, J. L. 1978 *Processing of Random Signals*, pp. 757–800.

Glauser, M. N. 1987 Coherent structures in the axisymmetric turbulent jet mixing layer. PhD thesis, State University of New York at Buffalo.

Glauser, M. N. & George, W. K. 1987 An orthogonal decomposition of the axisymmetric jet mixing layer utilizing cross-wise velocity measurements. In *Proc. Sixth Symp. Turb. Shear Flows*, pp. 10.1.1–10.1.6. Springer.

Glauser, M. N., Leib, S. J. & George, W. K. 1992 Application of multipoint measurements for flow characterization. *Expl Thermal Fluid Sci.* **5**, 617–632.

Glauser, M. N. & George, W. K. 1987 Coherent structures in the axisymmetric mixing layer. In *Turbulent Shear Flows 5* (ed. F. Durst *et al.*), p. 134. Springer.

Grinstein, F. F., Glauser, M. N. & George, W. K. 1995*a* Turbulent jets. In *Fluid Vortices* (ed. S. Green). Kluwer.

Grinstein, F. F., Gutmark, E. J., Parr, T. P., Hanson-Parr, D. M. & Obeysekare, U. 1995*b*

Streamwise and spanwise vortex interaction in a circular reacting jet – an experimental and computational study. In *Turb. Shear Flows X, Penn. State*.

Holmes, P., Lumley, J. L. & Berkooz, G. 1996 *Turbulence, Coherent Structures, Symmetry and Dynamical Systems*. Cambridge University Press.

Hussain, A. K. M. F. 1983 Coherent structures – reality and myth. *Phys. Fluids* **26**, 2816.

Hussain, A. K. M. F. 1986 Coherent structures and turbulence. *J. Fluid Mech.* **173**, 303–356.

Hussain, A. K. M. F. & Clark, A. R. 1981 On the coherent structure of the axisymmetric mixing layer: a flow-visualization study. *J. Fluid Mech.* **104**, 263–294.

Khwaja, Muhammed S. S. 1981 Investigation of the turbulent axisymmetric jet mixing layer. Master's thesis, State University of New York at Buffalo.

Lasheras, J. C., Cho, J. S. & Maxworthy, T. 1986 On the origin and evolution of streamwise vortical structures in a plane, free shear layer. *J. Fluid Mech.* **172**, 231–258.

Lau, J. C. & Fisher, M. J. 1975 The vortex-street structure of 'turbulent' jets. *J. Fluid Mech.* **67**, 299–337.

Liepmann, D. 1991 Streamwise vorticity and entrainment in the near-field of a round jet. *Phys. Fluids* A **3**, 1179–1187.

Liepmann, D. & Gharib, M. 1992 The role of streamwise vorticity in the near-field entrainment of round jets. *J. Fluid Mech.* **245**, 643–668.

Lim, T. T. 1997 A note on the leapfrogging between two coaxial vortex rings at low Reynolds numbers. *Phys. Fluids* **9**, 239–241.

Lin, S. J. & Corcos, G. M. 1984 The mixing layer: deterministic models of a turbulent flow. Part 3. The effect of plane strain on the dynamics of streamwise vortices. *J. Fluid Mech.* **141**, 139–178.

Lumley, J. L. 1967 The structure of inhomogeneous turbulent flows. In *Atmospheric Turbulence and Radio Wave Propagation* (ed. A. M. Yaglom & V. I. Tatarsky), pp. 166–178. Nauka, Moscow.

Lumley, J. L. 1970 *Stochastic Tools in Turbulence*. Academic.

Martin, J. & Meiburg, E. 1991 Numerical investigation of three-dimensionally evolving jets subject to axisymmetric and azimuthal perturbations. *J. Fluid Mech.* **230**, 271–318.

Metcalfe, R. W., Orszag, S. A., Brachet, M. E., Menon, S. & Riley, J. J. 1987 Secondary instability of a temporally growing mixing layer. *J. Fluid Mech.* **184**, 207–243.

Michalke, A. 1965 On spatially growing disturbances in an inviscid shear layer. *J. Fluid Mech.* **23**, 521–544.

Moin, P. & Moser, R. D. 1989 Characteristic-eddy decomposition of turbulence in a channel. *J. Fluid Mech.* **200**, 471–509.

Paschereit, C. O., Oster, D., Long, T. A., Fiedler, H. E. & Wygnanski, I. 1992 Flow visualization of interactions among large coherent structures in an axisymmetric jet. *Exps. Fluids* **12**, 189–199.

Perry, A. E. 1982 *Hot Wire Anemometry*. Clarendon.

Pierrehumbert, R. T. & Widnall, S. E. 1982 The two- and three-dimensional instabilities of a spatially periodic shear layer. *J. Fluid Mech.* **114**, 59–82.

Rogers, M. M. & Moser, R. D. 1992 The three-dimensional evolution of a plane mixing layer: the Kelvin–Helmholtz rollup. *J. Fluid Mech.* **243**, 183–226.

Sreenivasan, K. R. 1984 The azimuthal correlation of velocity and temperature fluctuations in an axisymmetric jet. *Phys. Fluids* **27**, 867–875.

Van Dyke, M. 1982 *An Album of Fluid Motion*. Parabolic Press, Stanford, California.

Widnall, S. E. & Sullivan, J. P. 1973 On the stability of vortex rings. *Proc. R. Soc. Lond.* A **332**, 335–353.

Winant, C. D. & Browand, F. K. 1974 Vortex pairing: the mechanism of turbulent mixing-layer growth at moderate Reynolds number. *J. Fluid Mech.* **63**, 237–255.

Yule, A. J. 1978 Large-scale structure in the mixing layer of a round jet. *J. Fluid Mech.* **89**, 413–432.

Zaman, K. B. M. Q. & Hussain, A. K. M. F. 1980 Vortex pairing in a circular jet under controlled excitation. Part 1. General jet response. *J. Fluid Mech.* **101**, 449–491.

Zaman, K. B. M. Q. & Hussain, A. K. M. F. 1984 Natural large-scale structures in the axisymmetric mixing layer. *J. Fluid Mech.* **138**, 325–351.

Zheng, X. & Glauser, M. N. 1991 A low-dimensional dynamical systems description of coherent structures in the axisymmetric jet mixing layer. *Tech. Rep.* MAE-247, Clarkson University.